New Inter- and Inner-Phase Power Control Method for Cascaded H-Bridge Based on Simplified PWM Strategy

Zongbin Ye, *Member, IEEE*, Qisheng Zheng, Hanjun Pei, Josep M. Guerrero, *Fellow, IEEE*, Shiqi Mao,
Tingting Wang, Anni Chen, Zhiguo Zhang, Linlin Jiang, Dongsheng Yu, *Member, IEEE*,
and Tyrone Fernando, *Senior Member, IEEE*

***Abstract*—Cascaded H-bridge (CHB) converters characterized with high scalability have been widely used in photovoltaic and energy storage systems. However, the three-phase power and the voltages are often unequal due to various reasons, making the system less efficient. Therefore, the ability to deal with unequal power is necessarily required in CHB. This article proposes three interphase power control methods (PCMs) based on simplified pulsewidth modulation (PWM) strategy to improve the efficiency of the system. A control method with better performance both in dynamic and steady states is adopted to adjust power distribution. The relationship between duration times and dc power is analyzed. On the basis of controlling the interphase power, an inner-phase PCM is proposed by redistributing the duration time of each submodule, to further enhance the power control ability of the system. The simulation and experimental results show that under the condition of balanced or unbalanced voltage, the interphase and inner-phase power can be controlled, which verifies the feasibility and practicability of several modulation strategies proposed in this article.**

***Index Terms*—DC–AC power conversion, multilevel systems, power control, pulsewidth modulation.**

I. INTRODUCTION

RENEWABLE energy sources such as wind and solar energy have attracted wide research attention, as the low-carbon economy is globally advocated. Photovoltaic (PV) power systems can realize clean electricity generation and hence reduce the dependence on fossil fuels [1]. For large PV generation systems, cascaded H-bridge (CHB) is regarded as one of the prime candidates for the lasted megawatt-class PV converters [2]–[4]. Compared with other topologies, CHB can provide smoother output voltage, better scalability, and low voltage stress on switches [5]–[8].

Despite the fact that CHB structure can achieve higher conversion efficiency and can be easily extended to more levels [9], it is confronted with the problem that the power generated by PV modules is often unbalanced [10]. This can be attributed to nonuniform solar irradiance, unequal temperature, inconsistent module degradation, and other factors [11], [12]. Similar problems also exist in the field of energy storage systems. In microgrid, SoC of energy storage systems is always unbalanced due to the difference in line impedances and the initial value of SoC [13]. Differences of SoC in energy storage systems will cause uneven power generation. Power imbalance, including interphase power imbalance and inner-phase power imbalance, will further result in the imbalance in three-phase currents, which, as delivered to the grid, may lead to the PV generation system disconnect from the gird [14].

To address this problem, several control strategies have been proposed. Injecting zero-sequence voltage can help to reduce dc power imbalance [15]. To simplify the computation, a novel weighting min–max zero-sequence voltage injection method is proposed in [16] and applied to grid-connected PV systems [17]. The zero sequence voltage in this method is equal to half of the sum of the maximum and minimum values, wherein the maximum and minimum values are obtained from the product of the power imbalance ratio and the corresponding voltage reference. Although this method can achieve power balance, it does not analyze the controllable range of power. In [10]–[12], an optimal zero sequence voltage injection method is proposed and applied to PV topologies. In this way, the problem of interphase power imbalance can be solved. However, the dc power in this method always deviates from the expected values because it equals the power on the grid side to the power on the converter side during the derivation process, making the power control inaccurate. Besides, the relationship between the linear modulation index and power generation ratios limitation, which is important for

Manuscript received February 5, 2019; revised May 4, 2019 and September 29, 2019; accepted December 11, 2019. Date of publication December 23, 2019; date of current version April 22, 2020. This work was supported by the Fundamental Research Funds for the Central Universities under Award 2019XKQYMS36. Recommended for publication by Associate Editor M. Tavakoli Bina. *(Corresponding author: Zongbin Ye.)*

Z. Ye, Q. Zheng, H. Pei, S. Mao, T. Wang, and D. Yu are with the School of Electrical and Power Engineering, China University of Mining and Technology, Xuzhou 221008, China (e-mail: yezongbin@163.com; w1373529836@163.com; 18772289282@163.com; 17851147002@163.com; wangtt_1994@163.com; dongsiee@163. com).

J. M. Guerrero is with the Department of Energy Technology, Aalborg University, Aalborg 9220, Denmark (e-mail: joz@et.aau.dk).

A. Chen is with the Zhongtian Construction Group Co., Ltd., Hangzhou 310020, China (e-mail: anne1993chen@163.com).

Z. Zhang is with the State Grid Yantai Power Supply Company, Yantai 264000, China (e-mail: zgwangyinet@163.com).

L. Jiang is with the State Grid Jiaxing Power Supply Company, Jiaxing 314000, China (e-mail: jianglinlin0410@163.com).

T. Fernando is with the School of Electrical, Electronic and Computer Engineering, University of Western Australia, Crawley, WA 6009, Australia (e-mail: tyrone.fernando@uwa.edu.au).

Color versions of one or more of the figures in this article are available online at http://ieeexplore.ieee.org.

Digital Object Identifier 10.1109/TPEL.2019.2961945

PV systems under different modulation index, is unclear. In [18], a scheme is proposed to induce an inverse imbalance proportional to power imbalance in the phase voltages, by modifying the converter neutral point voltage. Through this reverse imbalance, the imbalance of interphase power can be solved. However, there is significant fluctuation in power under this control method, meaning it does not achieve precise control. Besides, per cell power imbalance compensation is achieved by using PI control to modify the amplitude of the reference signal to redistribute the ON and OFF times of each cell. The problem with this method is that the response is slower compared to the interphase power balancing method. In [19], a predictive control method for grid-connected CHB converters under unbalanced power generation ratios is presented; it achieves power balance by enforcing the CHB converter to work with a suitable zero-sequence voltage component. This method simplifies the switch combination, for two-cell converters, but it still requires to evaluate 125 input combinations in the cost function to obtain the optimal one. The computing, therefore, is made rather complex. In [20], a simple dc-power control method (PCM) is proposed to tackle the imbalanced dc-power supply issue. This method can keep ac currents balance and maintain power generation ratio of each dc source at their expected value. With this method, the duration time of each phase is modified directly by the correction value derived from PCM. The superiority of the method is that it can control the dc power per phase accurately in variable-frequency condition, even under larger power generation ratios. However, power generation ratios fluctuate around their reference values, and the control accuracy needs to be improved.

The converters adopted in PV generally fall into two categories: central inverters and string inverters. As to central inverters, they have to balance the voltages and realize maximum power point tracking (MPPT) simultaneously. As to string inverters, a dc–dc converter is integrated into each inverter to realize MPPT and the inverter module deals with the unbalanced voltages. This makes it easier to gain a wider MPPT range than central inverters.

A high power plant requires a large quantity of string inverters to make parallel connections of their ac terminals, which will lead to a rise in current THD and even results in oscillation. Besides, the increase in the number of parallel inverters will cause a higher total failure rate. These problems can be solved at the expense of limited MPPT range and MPPT channels by using central converters. As we use the CHB as the PV inverter and adopt the suitable control strategy, it obtains a series of MPPT channels just like in string inverters and it can easily increase the power without deteriorating the current THD and failure rate.

This article proposes three interphase PCMs based on simplified pulsewidth modulation (PWM) modulation strategy [20] to achieve precise dc power control. In these methods, each phase or submodule is properly set to operate at different output power to improve the efficiency of the system and help achieving MPPT [17], [21]. Balanced three-phase currents can be obtained through imbalanced phase power distribution with these methods. In addition, an inner-phase PCM is proposed to further improve the power control capability of each submodule of the system. Also, this article gives the limitation and control range of power generation ratios. Variable dc voltage source is utilized to simulate the unbalanced PV module voltages effect in the experiment. The feasibility and practicability of power control are verified by comparing the experimental waveforms.

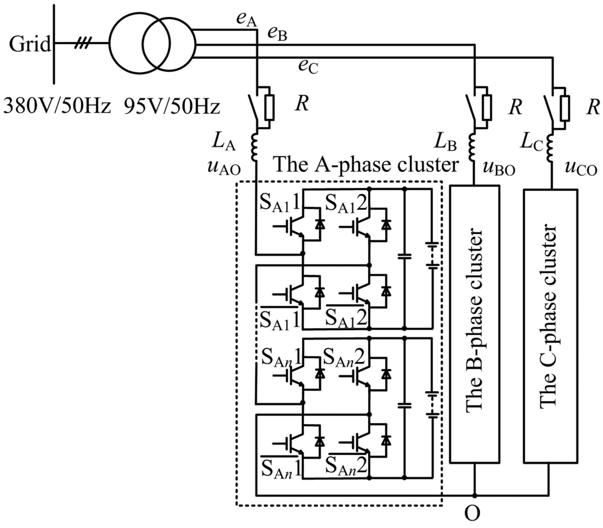

Fig. 1. Circuit of cascaded H-bridge converter.

The rest of this article is organized as follows. Section II introduces the simplified PWM strategy and the dc power calculation. Then, three interphase PCMs are derived in Section III and an inner-phase PCM is derived in Section IV. Section V analyzes the control limitation of power control. The simulations and experiments of a three-phase five-level CHB converter are conducted in Section VI. In Section VII, the final conclusion is drawn.

II. INTRODUCTION OF THE SIMPLIFIED PWM STRATEGY AND DC POWER CALCULATION

A. *Introduction of the Simplified PWM Strategy*

The circuit configuration of CHB is shown in Fig. 1. $U_{\mathrm{dc}\_Xi} (X = A, B, C; i = 1, 2, 3, \ldots, n)$ represents the dc-link voltage of submodule i of phase X, and it is set to be equal for the sake of analysis.

$$U_{\mathrm{dc}\_X_1} = U_{\mathrm{dc}\_X_2} = \cdots = U_{\mathrm{dc}\_X_n} = U_{\mathrm{dc}} (X = \mathrm{A},\ \mathrm{B},\ \text{or } C). \tag{1}$$

By referring to the voltage-second balancing principle discussed in [22], [23], three-phase duration times T'_X can be obtained, as shown in (2), where T_X represents the duration time of each phase before the correction time ΔT is added, $\Delta T\ (\Delta T = (u_{\mathrm{OO'}} \cdot T_{\mathrm{S}})/U_{\mathrm{dc}})$ represents the duration time of equivalent zero-sequence voltage

$$\begin{aligned} T'_X &= \left[\frac{u_{X\mathrm{ref}} T_{\mathrm{s}}}{U_{\mathrm{dc}}} + \frac{1 - \mathrm{sgn}(u_{X\mathrm{ref}})}{2} \cdot nT_{\mathrm{s}}\right] - \Delta T \\ &= T_X - \Delta T. \end{aligned} \tag{2}$$

The relationship between the duration time of each phase and the duration times of submodules can be expressed by (3), where T_{Xi} is the duration time of corresponding submodule.

$$T_X = T_{X_1} + T_{X_2} + \cdots + T_{X_n}. \tag{3}$$

The ΔT in (2) represents the correction value of T_X, and it can be used to achieve such targets as minimum pulsewidth compensation, switching losses reduction [22], linear modulation index extension [23]. And ΔT can also be used to achieve dc-power control with good performance and convenience [20]. However, it should be noted that the three effects, minimum pulsewidth compensation, switching losses reduction, and active power control, cannot be achieved in the meantime, since the pulse distribution methods of them are different. To realize the linear modulation, ΔT should satisfy (4), and the existent condition of ΔT can be expressed by inequality (5)

$$0 \le T'_X = T_X - \Delta T \le nT_s \tag{4}$$

$$\underbrace{\max(T_A, T_B, T_C) - nT_s}_{\Delta T_{\min}} \le \Delta T \le \underbrace{\min(T_A, T_B, T_C)}_{\Delta T_{\max}}. \tag{5}$$

B. DC Power Analysis and Calculation

In order to get higher control precision of dc power, this article employs a method based on the calculation of one carrier-wave period dc power.

1) Principle of Computing DC Power: Ignoring converter losses, the power calculated in the dc side is equal to the ac side. As the system is stable, the dc power per submodule in a fundamental period can be given by

$$\begin{cases} P_{\mathrm{A}_i} = \dfrac{1}{\mathrm{T}} \int_t^{t+\mathrm{T}} U_{\mathrm{dc\_A}_i} \cdot i_{\mathrm{dc\_}A_i} \mathrm{d}t \\ P_{\mathrm{B}_i} = \dfrac{1}{\mathrm{T}} \int_t^{t+\mathrm{T}} U_{\mathrm{dc\_}B_i} \cdot i_{\mathrm{dc\_}B_i} \mathrm{d}t \\ P_{\mathrm{C}_i} = \dfrac{1}{\mathrm{T}} \int_t^{t+\mathrm{T}} U_{\mathrm{dc\_C}_i} \cdot i_{\mathrm{dc\_C}_i} \mathrm{d}t \end{cases} \tag{6}$$

where $i_{\mathrm{dc\_}Xi}$ is the dc side current, $U_{\mathrm{dc\_}Xi}$ is the dc side voltage, i_X is the phase current, and S_{Xi} is the switching function of each submodule, satisfying $S_{Xi} = S_{Xi}1 - S_{Xi}2$, and T is the fundamental period

$$i_{\mathrm{dc\_}X_i} = i_X \cdot S_{X_i}. \tag{7}$$

Combining (6) with (7), introducing

$$P_{X_i} = \frac{1}{\mathrm{T}} \int_t^{t+\mathrm{T}} U_{\mathrm{dc\_}X_i} \cdot i_X \cdot S_{X_i} \mathrm{d}t. \tag{8}$$

Since the sampling frequency is high, the dc side voltages and currents ($U_{\mathrm{dc\_}Xi}$, $i_{\mathrm{dc\_}Xi}$) remain constant, then (6) can be rewritten as

$$P_{X_i} = \frac{1}{N} \sum_{k=0}^{N} p_{X_i}(k) \tag{9}$$

where

$$p_{X_i}(k) = U_{\mathrm{dc\_}X_i}(k) i_X(k) \cdot \left[T_X(k) - \frac{1 - \mathrm{sgn}(u_{X\mathrm{ref}}(k))}{2} \cdot nT_S - \Delta T(k) \right] \cdot \frac{1}{T_S} \tag{10}$$

$$N = \mathrm{floor}(\mathrm{T}/T_s) \tag{11}$$

where T represents the fundamental period, and T_{S} represents the carrier-wave period.

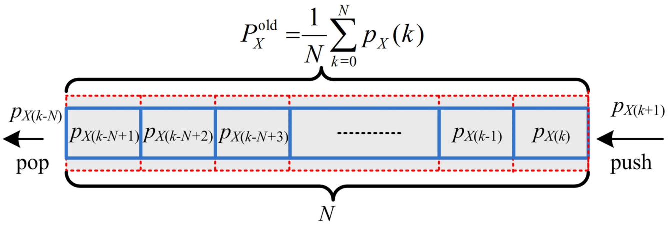

Fig. 2. Diagram of FIFO.

Equation (10) expresses the dc power generated by submodule *i* of phase *X* within T_{S}. Thus, the dc power generated by one phase within one fundamental period can be expressed by

$$P_X = \sum_{i=1}^{n} P_{X_i}. \tag{12}$$

By combining (9), (10), and (12), the dc power generated by one phase can be rewritten as

$$P_X = \frac{1}{N} \sum_{k=0}^{N} p_X(k) \tag{13}$$

where

$$p_X(k) = U_{\mathrm{dc\_}X}(k) i_X(k) \cdot \left[T_X(k) - \frac{1 - \mathrm{sgn}(u_{X\mathrm{ref}}(k))}{2} \cdot nT_S - \Delta T(k) \right] \cdot \frac{1}{T_S}. \tag{14}$$

Equation (14) represents the dc power generated by one phase within one carrier-wave period.

2) Method of Computing DC Power: A first-in first-out (FIFO) data queue is introduced to realize dc-power real-time calculation [20], as shown in Fig. 2. The length of queue depends on the proportion between the fundamental period and carrier-wave period and is set to *N* based on the above analysis. In each T_{S}, a new data which, calculated by (15), will be filled in the queue

$$p_X(k+1) = U_{\mathrm{dc\_}X}(k+1) i_X(k+1) \cdot \left[T_X(k+1) - \frac{1 - \mathrm{sgn}(u_{X\mathrm{ref}}(k+1)}{2} \cdot nT_S - \Delta T(k+1) \right] \cdot \frac{1}{T_S}. \tag{15}$$

The dc power average power P_X^{new} will be updated as

$$P_X^{\mathrm{new}} = P_X^{\mathrm{old}} + \frac{1}{N}[p_X(k+1) - p_X(k{-}N+1)] \tag{16}$$

where P_X^{new} is the average power after updating, and P_X^{old} is the average power of the previous cycle.

3) Relationship Between Power Generation Ratios and DC Power: The average dc power of three phases can be expressed by

$$P_{\mathrm{ave}} = \frac{(P_A + P_B + P_C)}{3}. \tag{17}$$

Thus, the power generation ratios $k_X (X = A, B, C)$ given by (18) should satisfy (19)

$$k_A = \frac{P_A}{P_{\mathrm{ave}}}, k_B = \frac{P_B}{P_{\mathrm{ave}}}, k_C = \frac{P_C}{P_{\mathrm{ave}}} \tag{18}$$

$$k_A + k_B + k_C = 3. \tag{19}$$

Equation (20) shown at the bottom of this page, can be obtained by substituting (2), (13), and (14) into (17).

In three-phase symmetry power systems, the sum of the three-phase currents is zero, so term II of (20) is zero. Thus, P_{ave} is only determined by dc-link voltages $U_{\mathrm{dc\_}X}$ and ac currents i_X, while ΔT has no effect on it. Equation (21) shown at the bottom of this page, which acquired by substituting (13) and (20) into (18) illustrates the relationship between k_X and ΔT. The derivation process is presented in (21), where P_X^0 represents the power of each phase before we control the power. In balanced three-phase symmetry power systems, P_X^0 is equal to P_{ave}.

As can be seen from (21), power generation ratios k_X is only related to three variables as dc side voltages $U_{\mathrm{dc\_}X}$, ac side currents i_X, and duty ratio correction ΔT, so the dc power can be controlled by adjusting correction value ΔT. This adjustment does not affect the average dc power of the converter.

III. Three Interphase Power Control Methods

Based on the above analysis, the dc power can be controlled by adjusting the correction value ΔT. Thus, the control accuracy depends on the precision of ΔT. The three calculation methods are presented as follows.

A. Control Method Based on the Minimum and Maximum Values of ΔT (CMMM)

The following steps outline CMMM when $k_X \neq k_X^*$, where k_X^* is the references of dc power ratios.

1) Choosing the Priority Control Phase: The power generation ratio deviation is defined as $\Delta k_X = |k_X^* - k_X|$. Since the phase with the largest value of Δk_X deviates maximally, it will be set as the priority control phase. And the direction of ΔT will be decided by

$$\begin{array}{ll} \text{if } \Delta k_A = \max(\Delta k_A, \Delta k_B, \Delta k_C), & \Delta T \text{ decided by A} \\ \text{if } \Delta k_B = \max(\Delta k_A, \Delta k_B, \Delta k_C), & \Delta T \text{ decided by B} \\ \text{if } \Delta k_C = \max(\Delta k_A, \Delta k_B, \Delta k_C), & \Delta T \text{ decided by C.} \end{array} \tag{22}$$

2) Comparing the Expected Power Generation Ratios and Real Power Generation Ratios: By comparing k_X with k_X^*, to

$$\begin{aligned} P_{\mathrm{ave}} &= \frac{1}{3N} \sum_{k=0}^{N} \sum_{X=\mathrm{A,B,C}} \left\{ \frac{U_{\mathrm{dc\_}X}(k) i_X(k)}{T_S} \cdot \left[T_X(k) - \Delta T(k) - \frac{1 - \mathrm{sgn}[u_{X\mathrm{ref}}(k)]}{2} \cdot nT_S \right] \right\} \\ &= \underbrace{\frac{1}{3N} \sum_{k=0}^{N} \sum_{X=\mathrm{A,B,C}} \left\{ U_{\mathrm{dc\_}X}(k) i_X(k) \cdot \left[T_X(k) - \frac{1 - \mathrm{sgn}(u_{X\mathrm{ref}}(k))}{2} \cdot nT_S \right] \cdot \frac{1}{T_S} \right\}}_{\mathrm{termI}} \\ &\quad \underbrace{- \frac{1}{3N} \sum_{k=0}^{N} U_{\mathrm{dc}}(k) \cdot \Delta T(k) \frac{1}{T_S} \sum_{X=\mathrm{A,B,C}} i_X(k)}_{\mathrm{termII}} \end{aligned} \tag{20}$$

$$\begin{aligned} & P_X = k_X P_{\mathrm{ave}} \\ & \quad \Downarrow \\ & \frac{1}{N} \sum_{k=0}^{N} \left\{ U_{\mathrm{dc\_}X}(k) i_X(k) \cdot \left[T_X(k) - \frac{1 - \mathrm{sgn}(u_{X\mathrm{ref}}(k))}{2} \cdot nT_S - \Delta T(k) \right] \cdot \frac{1}{T_S} \right\} \\ & \qquad = k_X \frac{1}{3N} \sum_{k=0}^{N} \sum_{X=\mathrm{A,B,C}} \left\{ U_{\mathrm{dc\_}X}(k) i_X(k) \cdot \left[T_X(k) - \frac{1 - \mathrm{sgn}(u_{X\mathrm{ref}}(k))}{2} \cdot nT_S \right] \cdot \frac{1}{T_S} \right\} \\ & \quad \Downarrow \\ & P_X^0 - \frac{1}{N} \sum_{k=0}^{N} \left[U_{\mathrm{dc\_}X}(k) i_X(k) \cdot \Delta T\,(k) \cdot \frac{1}{T_S} \right] = k_X P_{\mathrm{ave}} \\ & \quad \Downarrow \\ & \frac{1}{N} \sum_{k=0}^{N} \left[U_{\mathrm{dc\_}X}(k) i_X(k) \cdot \Delta T\,(k) \cdot \frac{1}{T_S} \right] = (1 - k_X) P_{\mathrm{ave}} \end{aligned} \tag{21}$$

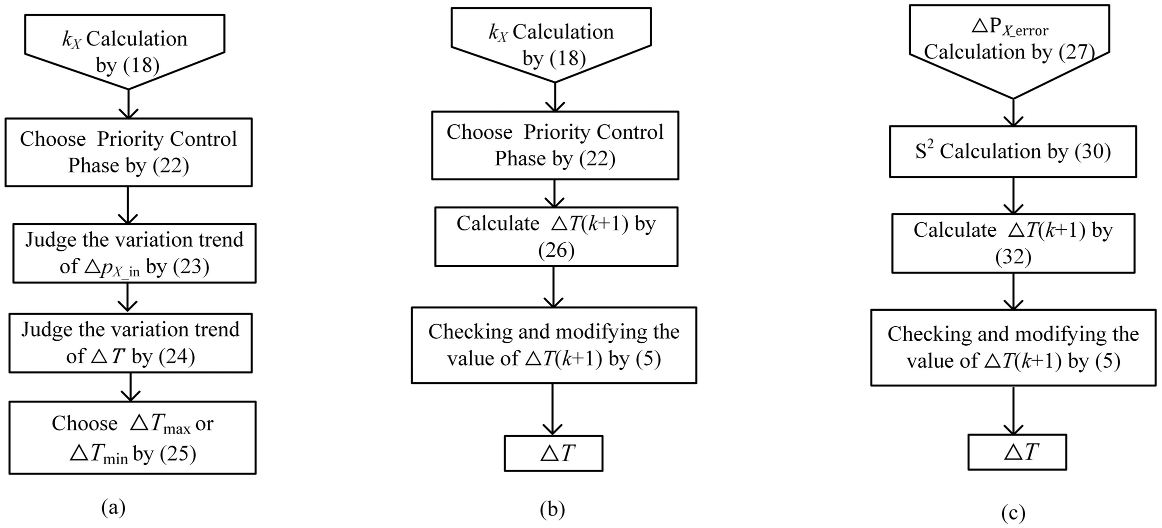

Fig. 3. Flow chart of proposed methods. (a) CMMM. (b) CMPP. (c) CMMV.

increase or decrease $p_X(k+1)$ can be determined. For example, when k_X is greater than k_X^*, the output power p_X of each phase is less than zero. In order to reach the expected value, p_X should be increased. Thus, $p_X(k+1)$ will be decided by (23) based on

$$\begin{cases} \text{if } k_X > k_X^*, & \Delta P_X^{\text{current}} \text{ to be increased} \\ & \qquad \Rightarrow \Delta p_{X\_\text{in}} \text{ to be increased} \\ \text{if } k_X < k_X^*, & \Delta P_X^{\text{current}} \text{ to be decreased} \\ & \qquad \Rightarrow \Delta p_{X\_\text{in}} \text{ to be increased.} \end{cases} \tag{23}$$

3) Identifying the Direction of ΔT in Current Control Period: Since the direction of Δp_{X_in} has been decided by step *2)*, the variation trend of ΔT in current control period is expressed by (24) based on (16).

$$\text{if } k_X > k_X^* \begin{cases} \text{if } \operatorname{sgn}(i_X) > 0, & \begin{matrix} \Delta p_{X\_\text{in}} \text{ to be increased} \\ \Downarrow \\ \Delta T \text{ to be increased} \end{matrix} \\ \text{if } \operatorname{sgn}(i_X) < 0, & \begin{matrix} \Delta p_{X\_\text{in}} \text{ to be increased} \\ \Downarrow \\ \Delta T \text{ to be decreased} \end{matrix} \end{cases} \tag{24-a}$$

$$\text{if } k_X < k_X^* \begin{cases} \text{if } \operatorname{sgn}(i_X) > 0, & \begin{matrix} \Delta p_{X\_\text{in}} \text{ to be decreased} \\ \Downarrow \\ \Delta T \text{ to be decreased} \end{matrix} \\ \text{if } \operatorname{sgn}(i_X) < 0, & \begin{matrix} \Delta p_{X\_\text{in}} \text{ to be decreased} \\ \Downarrow \\ \Delta T \text{ to be increased.} \end{matrix} \end{cases} \tag{24-b}$$

4) Identifying the Value of ΔT in Current Control Period: According to the previous analysis, the range of ΔT is [$\Delta T_{\min}$ $\Delta T_{\max}$]. So the value of ΔT is decided by

$$\begin{aligned} &\text{if } \Delta T \text{ to be increased} \Rightarrow \Delta T = \Delta T_{\max} \\ &\text{if } \Delta T \text{ to be decreased} \Rightarrow \Delta T = \Delta T_{\min}. \end{aligned} \tag{25}$$

So far, CMMM algorithm has been fulfilled and the flow chart of CMMM is shown in Fig. 3(a).

B. Control Method based on the Control Priority Phase (CMPP)

CMMM is intuitive, but there is no unified formula to calculate the ΔT. So we analyze the relationship between ΔT and power generation ratios and give a formula for ΔT.

1) Choosing the Control Priority Phase: The first step is to choose the priority control phase used to calculate the ΔT, which is the same as CMMM.

2) Calculating the Value of ΔT: To achieve the interphase power control, we calculate the $\Delta T\,(k+1)$ to make the actual power equal to the expected one.

By combining (15), (16), and (18), $\Delta T\,(k+1)$ can be acquired by

$$\begin{aligned} \Delta T\,(k+1) = T_X\,(k+1) - \frac{1-\operatorname{sgn}[u_{X\text{ref}}\,(k+1)]}{2} nT_S \\ - \frac{T_S[N(k_X^* P_{\text{ave}} - P_X^{\text{old}}) + p_X\,(k-N+1)]}{U_{\text{dc}\_X}\,(k+1)\, i_X\,(k+1)}. \end{aligned} \tag{26}$$

3) Checking and Modifying the Value of ΔT: $\Delta T(k+1)$ should satisfy (5) to comply with linear modulation. When $\Delta T(k+1)$ reaches the limit of the [$\Delta T_{\min}$ $\Delta T_{\max}$], it should take the value of $\Delta T_{\min}$ or $\Delta T_{\max}$ accordingly. So far, CMPP algorithm can be fulfilled and the flow chart of CMPP is shown in Fig. 3(b).

C. Control Method Based on Minimizing the Variances of Three-Phase Power (CMMV)

In order to gain better steady-state performance of dc power control, $\Delta T(k+1)$ should precisely satisfy the three-phase power generation ratios simultaneously. Thus, $\Delta T(k+1)$ can be calculated by minimizing the variances of the three-phase power.

$\Delta P_{X\_\mathrm{error}}$ is the error between the actual and the expected power of each phase. CMMV is presented as follows.

$\Delta P_{X\_\mathrm{error}}$ can be expressed by

$$\Delta P_{X\_\mathrm{error}} = P_X^{\mathrm{old}} + \frac{1}{N}\left[p_X\,(k+1) - p_X\,(k{-}N+1)\right] - k_X^{*} P_{\mathrm{ave}}. \tag{27}$$

Thus, the variance of three-phase power is given by

$$\begin{aligned}\mathrm{S}^2 &= \Delta P_{\mathrm{A\_error}}{}^2 + \Delta P_{\mathrm{B\_error}}{}^2 + \Delta P_{\mathrm{C\_error}}{}^2\\ &= \left(P_A^{\mathrm{old}} + \frac{1}{N}\left[p_A\,(k+1) - p_A\,(k{-}N+1)\right] - k_A^{*}P_{\mathrm{ave}}\right)^2\\ &\quad + \left(P_{\mathrm{B}}^{\mathrm{old}} + \frac{1}{N}\left[p_{\mathrm{B}}\,(k+1) - p_B\,(k{-}N+1)\right] - k_B^{*}P_{\mathrm{ave}}\right)^2\\ &\quad + \left(P_C^{\mathrm{old}} + \frac{1}{N}\left[p_C\,(k+1) - p_C\,(k{-}N+1)\right] - k_C^{*}P_{\mathrm{ave}}\right)^2.\end{aligned} \tag{28}$$

According to (15), $p_X(k+1)$ can be expressed as

$$p_X\,(k+1) = u^{*}{}_{X\mathrm{ref}}(k+1)i_X(k+1) - \frac{U_{\mathrm{dc}}(k+1)i_X(k+1)\Delta T(k+1)}{T_S}. \tag{29}$$

Thus, (28) can be rewritten as (30) shown at the bottom of this page.

Equation (30) indicates that S^2 is a quadratic function of $\Delta T(k+1)$, and the opening is upward, so that the minimum duty ratio of the squared sum of the above power deviation is the duty ratio correction sought, namely, the extreme point above function. Thus, the extreme point can be acquired by (31), and can be simplified as (32) shown at the bottom of this page. ΔT can be used to control the dc power directly after a threshold processing

$$\frac{d(\mathrm{S}^2)}{d(\Delta T)} = 0 \tag{31}$$

So far, three algorithms have been fulfilled and the flow charts are shown in Fig. 3.

IV. Inner-Phase Power Control Method

Unbalanced power not only exists in interphase but also comes out in inner phase. Thus, there is a need for a method that can control the power distribution of the inner phase to further improve the power controllability of the system. This article proposes an inner-phase PCM to achieve power distribution by using the inner-phase duration correction value ΔD_{Xi}, which is similar to the interphase PCMs.

The inner-phase power generation ratios can be expressed as (33), where $P_{X\mathrm{ave}}$ is the average power of all submodules in a phase, P_{Xi} represents the dc power of submodule *i* of phase *X* in a fundamental period

$$l_{Xi} = \frac{P_{Xi}}{P_{X\ \mathrm{ave}}}. \tag{33}$$

According to (14), the revised duration time of one phase can be expressed as

$$D(X) = T_X(k) - \frac{1 - \mathrm{sgn}(u_{X\mathrm{ref}}(k))}{2}\cdot nT_S - \Delta T(k). \tag{34}$$

When the duration times distribute equally among the submodules, the dc power generated by one submodule within T_{s} can be expressed as (35), where ΔD_{Xi} is the correction value injected in submodule *i* of phase *X*, and it should satisfy $\Delta D_{X1} + \Delta D_{X2} + \cdots + \Delta D_{Xn} = 0$, so as not to affect the duration time of one phase

$$p_{Xi}(k) = U_{\mathrm{dc}}(k)i_{Xi}(k)\cdot\left[\frac{D(X)}{n} - \Delta D_{Xi}(k)\right]\cdot\frac{1}{T_s}. \tag{35}$$

Similar to the interphase power control, the relationship between the carrier-wave period dc power and the fundamental period dc power can be expressed as

$$p_{Xi}\,(k+1) = N(P_{Xi}^{*} - P_{Xi}^{\mathrm{old}}) + p_{Xi}\,(k{-}N+1)\,. \tag{36}$$

$$\begin{aligned}\mathrm{S}^2 = &\left(\left(P_A^{\mathrm{old}} + \frac{\left[u^{*}{}_{\mathrm{Aref}}(k+1)i_A(k+1) - \frac{U_{\mathrm{dc}}(k+1)i_A(k+1)\Delta T(k+1)}{T_S} - p_A\,(k{-}N+1)\right]}{N} - k_A^{*}P_{\mathrm{ave}}\right)\right)^2\\ &+\left(\left(P_B^{\mathrm{old}} + \frac{\left[u^{*}{}_{\mathrm{Bref}}(k+1)i_B(k+1) - \frac{U_{\mathrm{dc}}(k+1)i_B(k+1)\Delta T(k+1)}{T_S} - p_B\,(k{-}N+1)\right]}{N} - k_B^{*}P_{\mathrm{ave}}\right)\right)^2\\ &+\left(\left(P_C^{\mathrm{old}} + \frac{\left[u^{*}{}_{\mathrm{Cref}}(k+1)i_C(k+1) - \frac{U_{\mathrm{dc}}(k+1)i_C(k+1)\Delta T(k+1)}{T_S} - p_C\,(k{-}N+1)\right]}{N} - k_C^{*}P_{\mathrm{ave}}\right)\right)^2\end{aligned} \tag{30}$$

$$\begin{aligned}\Delta T(k+1) = &\frac{T_S N}{\mathrm{U}_{\mathrm{dc}}(i_A(k+1)^2 + i_B(k+1)^2 + i_C(k+1)^2)}\\ &* \begin{pmatrix}(P_A^{\mathrm{old}}i_A(k+1) + P_B^{\mathrm{old}}i_B(k+1) + P_C^{\mathrm{old}}i_C(k+1)\\ +\frac{1}{N}[u^{*}{}_{\mathrm{Aref}}(k+1)i_A(k+1) - p_A\,(k{-}N+1)] * i_A(k+1) - k_A^{*}P_{\mathrm{ave}} * i_A(k+1)\\ +\frac{1}{N}[u^{*}{}_{\mathrm{Bref}}(k+1)i_B(k+1) - p_B\,(k{-}N+1)] * i_B(k+1) - k_B^{*}P_{\mathrm{ave}} * i_B(k+1)\\ +\frac{1}{N}[u^{*}{}_{\mathrm{Cref}}(k+1)i_C(k+1) - p_C\,(k{-}N+1)] * i_C(k+1) - k_C^{*}P_{\mathrm{ave}} * i_C(k+1)\end{pmatrix}\end{aligned} \tag{32}$$

Combining (33), (35), and (36), the correction value of each submodule can be expressed as

$$\Delta D_{Xi}(k+1) = \frac{D(X)}{n} - \frac{N(l_{Xi}^{*}P_{X\text{ave}} - P_{Xi}^{\text{old}}) + p_{Xi}\,(k-N+1)}{U_{\text{dc}}(k+1)i_{Xi}(k+1)}T_s. \tag{37}$$

Therefore, the correction values can be obtained according to the inner-phase power generation ratios l_{Xi}^{*}, and it can be used to control the inner-phase power directly without affecting the interphase power.

Briefly, the inner-phase power control is achieved by changing the pulse distribution of each submodule. However, it should be noted that adopting interphase and inner-phase power control will lead to the increase of the switching frequency.

V. CONTROL LIMITATION OF POWER GENERATION RATIOS

With three interphase PCMs, power generation ratio of each phase will be distributed following the expected value, but the power regulation range is limited. The limitation will be analyzed to ensure the expansibility and applicability.

From (21), the adjustable dc power within one control period is shown as (38). According to (22), interphase power control can be achieved through controlling and adjusting ΔT

$$\Delta p_X(k) = U_{\text{dc\_}X}(k)i_X(k)\cdot \Delta T(k)/T_S. \tag{38}$$

Thus, the adjustable dc power ΔP_X within T_{fund} can be expressed as

$$\Delta P(k) = \frac{1}{N}\sum_{\text{k}=0}^{N}\Delta p_X(k). \tag{39}$$

Power generation ratios k_X in (18) can be rewritten as

$$k_X = \frac{P_{\text{ave}} - \Delta P_X}{P_{\text{ave}}}. \tag{40}$$

Therefore, ranges of ΔP_X will be analyzed to obtain the power generation ratios limitation.

For simplicity, the upper and lower limit of ΔP_{A} can be obtained assuming $\text{sgn}(u_{\text{A\_ref}}) = \text{sgn}(i_{\text{A}})$ and $k_A > k_A^{*}$. Therefore, (41) can be established to derive the limitation of ΔP_{A} based on (32), (38), and (39)

$$\Delta T_j = \begin{cases} \Delta T_{\max}, \text{sgn}(i_A) = 1/0 \\ \Delta T_{\min}, \text{sgn}(i_A) = -1. \end{cases} \tag{41}$$

The maximum value $\Delta P_{\text{max\_A}}$ can be expressed by

$$\begin{aligned} \Delta P_{\max\_A} &= \frac{1}{\text{T}}\int_0^{\pi} U_{\text{dc\_}A}\frac{u_{\text{Aref}}}{Z}\cdot \Delta T_{\max}\text{d}\omega\text{t} \\ &\quad + f_{\text{fund}}\int_{\pi}^{2\pi} U_{\text{dc\_}A}\frac{u_{\text{Aref}}}{Z}\cdot \Delta T_{\min}\text{d}\omega\text{t} \\ &= \underbrace{\frac{1}{\text{T}}\int_0^{\pi} U_{\text{dc\_}A}\frac{U_{\text{dc\_A}}m\text{sin}\,(\omega\text{t})}{Z}\cdot \Delta T_{\max}\text{d}\omega\text{t}}_{\text{Term 1}} \\ &\quad + \underbrace{\frac{1}{\text{T}}\int_{\pi}^{2\pi} U_{\text{dc\_}A}\frac{U_{\text{dc\_A}}m\text{sin}\,(\omega\text{t})}{Z}\cdot \Delta T_{\min}\text{d}\omega\text{t}}_{\text{Term 2}} \end{aligned} \tag{42}$$

where Z is the impedance of the grid side, and u_{Aref} ($u_{\text{Aref}} = U_{\text{dc\_A}}.m\cdot\text{sin}(\omega t)$) is the reference signal of phase A

$$\begin{aligned} \Delta T_{\max} &= \min(T_A, T_B, T_C) \\ &= \min\left\{ mT_s\text{sin}\,(\omega\text{t}) + \frac{1-\text{sgn}[\text{sin}\,(\omega\text{t})]}{2}\cdot nT_s \right. \\ &\quad \times mT_s\text{sin}\,(\omega\text{t} - 2\pi/3) + \frac{1-\text{sgn}[\text{sin}\,(\omega\text{t} - 2\pi/3)]}{2}\cdot nT_s \\ &\quad \left. \times\ mT_s\text{sin}\,(\omega\text{t} + 2\pi/3) + \frac{1-\text{sgn}[\text{sin}\,(\omega\text{t} + 2\pi/3)]}{2}\cdot nT_s \right\}. \end{aligned} \tag{43}$$

By analyzing (42) and (43), it can be found that term 1 and *m* can be related in quadratic function after the integral calculation. Term 2 can also be analyzed similarly. Consequently, $\Delta P_{\text{max\_A}}$ and *m* obey (45), where a, b, and c are coefficients

$$\text{Term 1} = \frac{1}{\text{T}}\int_0^{\pi} U_{\text{dc\_}A}\frac{U_{\text{dc\_A}}m\text{sin}\,(\omega\text{t})}{Z} \cdot \min(T_A, T_B, T_C)\text{d}\omega\text{t} \tag{44}$$

$$\Delta P_{\max\_A} = \text{a}m^2 + \text{b}m + \text{c}. \tag{45}$$

P_{ave} is a quadratic function of *m*, as shown in (46). So the relation of $k_{\min\_A}^{*}$ and *m* can be expressed by (47). Adopting the same method, $k_{\max\_A}^{*}$ can be easily attained as well

$$P_{\text{ave}} = \text{d}m^2 \tag{46}$$

$$k_{\min\_A}^{*} = \frac{P_{\text{ave}} - \Delta P_{\max\_A}}{P_{\text{ave}}} = \left(1 - \frac{\text{a}}{\text{d}}\right) - \frac{\text{b}}{\text{d}m} - \frac{\text{c}}{\text{d}m^2}. \tag{47}$$

According to (47), power generation ratio is a quadratic function of the reciprocal 1/*m*. Three special power points can be used to solve (47). The relationship between *m* and three-phase generation ratios are drawn in Fig. 4. Fig. 4(a) shows the corresponding relationship between the limit of the reference generation ratio $k_X^{*}(X = \text{A or B or C})$ and *m,* indicating that the reference generation ratio of each phase is acceptable within this range. At the same time, three-phase generation ratios must satisfy (19). In order to show the relationship between k_X^{*} and *m* as well as the three-phase generation ratios at the same time, a 3-D graph is drawn, as in Fig. 4(b). This 3-D graph is obtained by fitting the simulation data, since a unified mathematical expression has not been found at present. It can be seen that when *m* is 1, three-phase power generation ratios concentrate in the middle area of the 3-D graph, so the adjustable range is small. When *m* is 0.5, three-phase power generation ratios are distributed around the 3-D graph, so the adjustable range is large. It can be concluded that the active power control capability becomes weaker as modulation index *m* increases.

It is observed from the above analysis that the theoretical power generation ratios limitation is determined by modulation

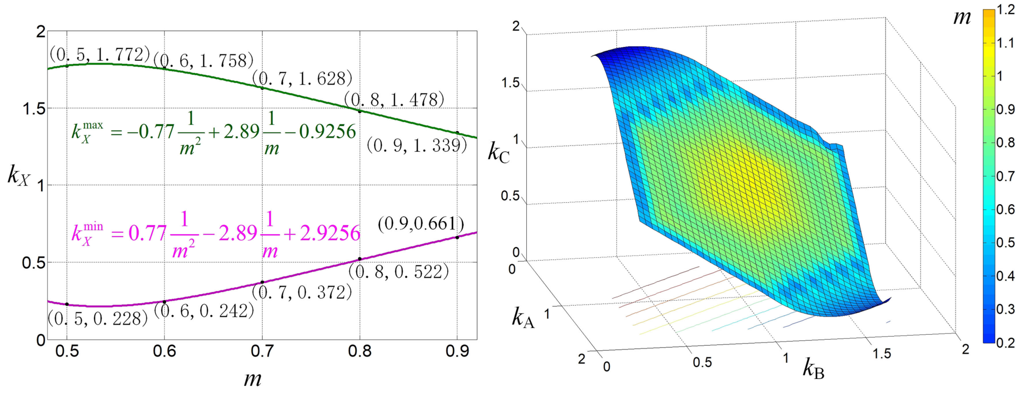

(a) (b)

Fig. 4. Limit of the reference power generation ratios $k{*}_X$. (a) Two-dimensional graph. (b) Three-dimensional graph.

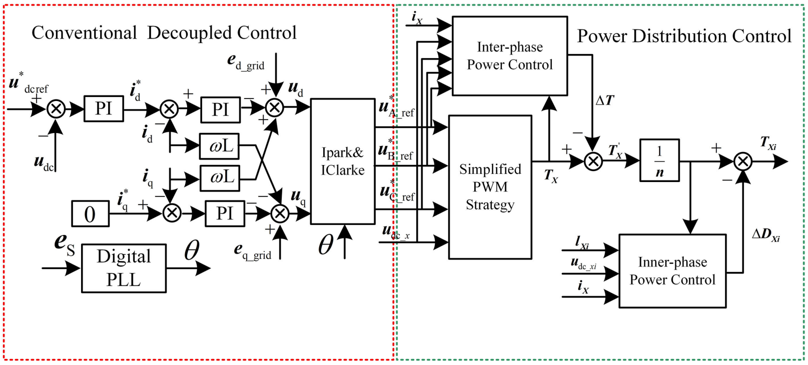

Fig. 5. Control block diagram of the grid-connected inverter system.

index m. If only the power generation ratios are within this theoretical range, the dc power can be controlled as expected.

VI. SIMULATION AND EXPERIMENT

Fig. 5 shows the control block diagram of grid-connected inverter. The whole control is divided into two subs controls: 1) conventional decoupled control based on the dq rotational frame; and 2) power distribution control using proposed methods.

A. Simulation and Analysis

1) Simulation Results of CMMM, CMPP, and CMMV in Low Power Systems: A three-phase five-level CHB grid-connected inverter is simulated in MATLAB/Simulink to compare the proposed three methods. The system parameters are shown in Table I and the simulation results are shown in Fig. 6.

TABLE I
PARAMETER SETTINGS FOR SIMULATIONS AND EXPERIMENTS IN LOW POWER SYSTEMS

Parameter	Value
Voltage of Battery Cells	48 V
DC-link Capacitor	1200 μF
L filter	4 mH
Switching Frequency	8 kHz
Chain number per phase	2
Rated Power	465 W

Fig. 6(a)–(c) show the simulation waveform of CMMM, CMPP, and CMMV with the power generation ratios ranging from $(k_A^*/k_B^*/k_C^* = 0.8/1/1.2)$ to $(k_A^*/k_B^*/k_C^* = 1.2/1/0.8)$, where the modulation index m is 0.89 and the output active power is 465 W. As can be seen from Fig. 6(a)–(c), the three PCMs can reach the expected power generation ratios, in which CMMM and CMPP can achieve fast control, while CMMV is more precise and smoother. This can be explained by Fig. 6(d)–(f) which shows the waveforms of correction time ΔT in the steady state. It should note that the value of ΔT is shown in red line, and the maximum and minimum allowable values of ΔT are shown in blue line, as observed using a uniform zero baseline. In Fig. 6(d), the waveform of ΔT switches between the upper and lower limits, causing the real-time dc power in CMMM to fluctuate. Power control with CMPP, as in Fig. 6(e), is not smooth, for the correction time ΔT always exceeds the limiting value and thus should be limited. In Fig. 6(f), ΔT falls within the limiting values and is continuous, indicating that ΔT can satisfy the three-phase power equation in CMMV. It is then concluded that CMMV can realize more accurate and smoother control of dc power. In addition, CMMM and CMPP select the phase whose power deviation is largest as the priority control phase, thus the fast control can be obtained. Since CMMV is a method that minimizes the total deviation of three-phase power,

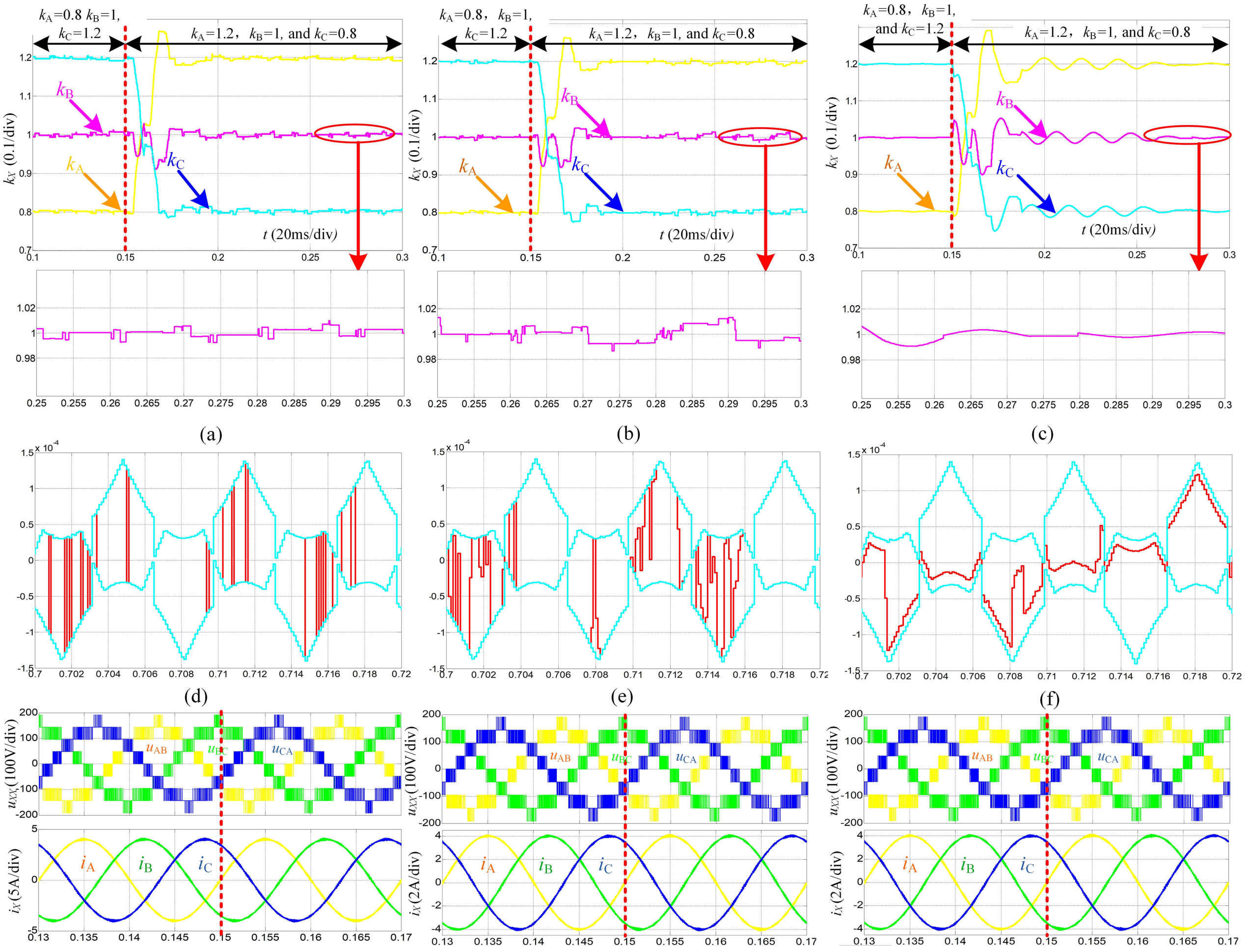

(a) (b) (c)

(d) (e) (f)

(g) (h) (i)

Fig. 6. Simulation results in low power systems with CMMM, CMPP, and CMMV, respectively. (a)–(c) Power generation ratios k_X. (d)–(f) Steady-state waveform of ΔT. (g)–(i) Converter output voltages u_{XX} and output ac currents i_X.

it takes more time to reach the steady state. Fig. 6(g)–(i) shows the waveforms of line-to-line voltages u_{XX} and ac currents i_X of CMMM, CMPP, and CMMV, respectively. It indicates that the high-quality voltages and currents can be obtained with these methods, and the switching of power generation ratios has little effect on them.

2) Simulation Results of CMMM, CMPP, and CMMV in High Power Systems: To verify the feasibility of three inter-phase PCMs in high power systems, the simulations with power generation ratios ranging from $(k_A^*/k_B^*/k_C^* = 1.2/1/0.8)$ to $(k_A^*/k_B^*/k_C^* = 0.8/1/1.2)$ are implemented in the 10-cell CHB converter, where the modulation index *m* is 0.89 and the output active power is 10MW. The simulation parameters are shown in Table II and the simulated results are shown in Fig. 7. It is clear from the figures that three control methods can achieve high precise control of dc power, and the simulation results are similar to those in low power systems.

Comparing the above simulation results, we find that, among three interphase PCMs, the performances in the dynamic and steady states differ. Table III illustrates their differences by presenting the main characteristics of the three methods.

TABLE II
PARAMETER SETTINGS FOR SIMULATIONS IN HIGH POWER SYSTEMS

Parameter	Value
Voltage of Battery Cells	577 V
DC-link Capacitor	1200 μF
L filter	4 mH
Switching Frequency	8 kHz
Chain number per phase	10
Rated Power	10 MW

3) Simulation Results of the Method Merging CMPP and CMMV (MCC): In order to obtain good performance both in dynamic and steady states, the CMPP and CMMV are combined to form a new control strategy MCC.

By analyzing the variances of three-phase power S^2, we find that 0.01 is the critical point which can be used to decide the control strategy switch point. When S^2 is greater than 0.01, ΔT is calculated using CMMP. Otherwise, the CMMV is adopted to acquire the ΔT. The flow chart of method MCC is shown in Fig. 8.

The simulation is conducted in a five-level CHB grid-connected inverter. Table I and Fig. 9 show the simulation

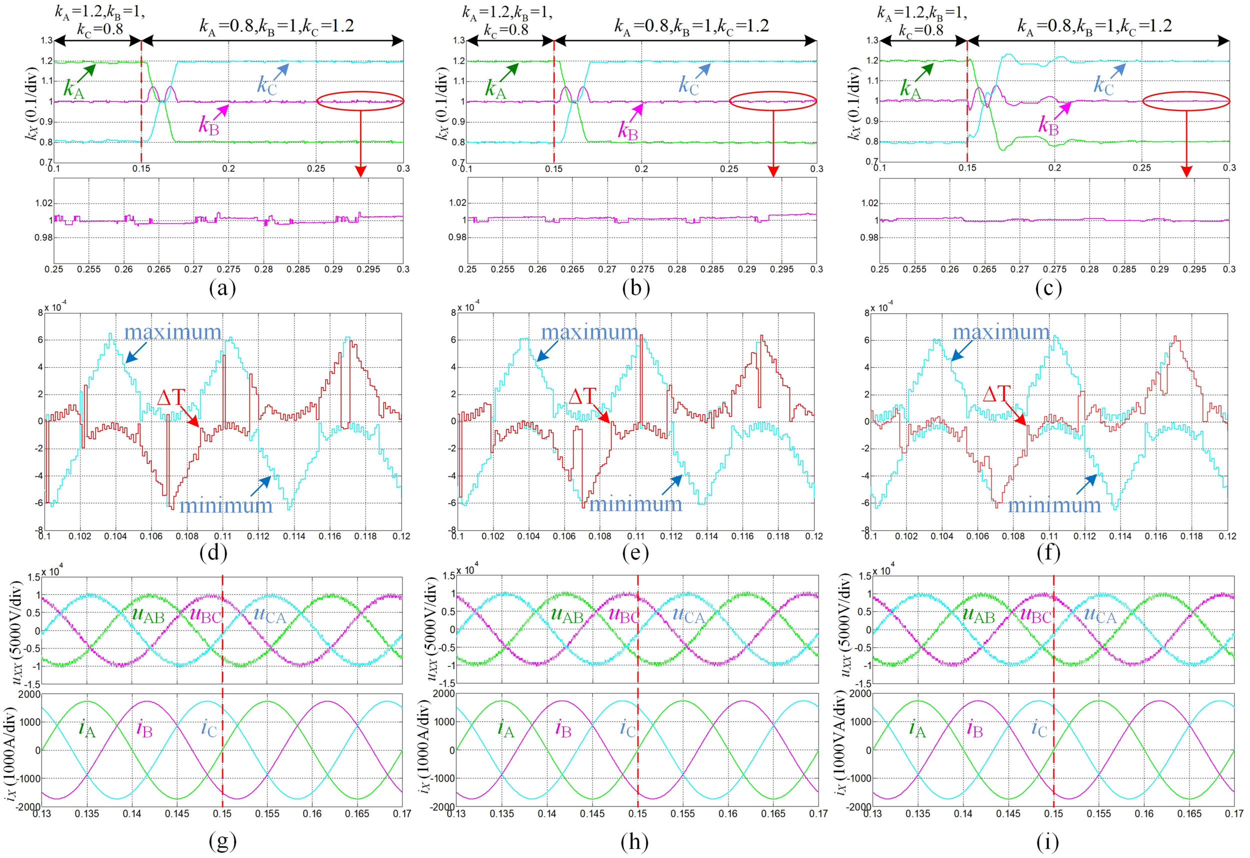

Fig. 7. Simulation results in high power systems with CMMM, CMPP, and CMMV, respectively. (a)–(c) Power generation ratios k_X. (d)–(f) Steady-state waveform of ΔT. (g)–(i) Converter output voltages u_{XX} and output ac currents i_X.

TABLE III
DIFFERENCES AMONG THREE INTERPHASE POWER CONTROL METHODS

Difference	CMMM	CMPP	CMMV
Stable speed	Rapid (0.05 s)	Rapid (0.03 s)	relatively slow(0.11 s)
Stable state	slight fluctuation	slight fluctuation	smooth
Control precision	slight deviation(±0.01)	slight deviation(±0.015)	high precision(±0.003)

parameters and the simulation results, respectively, to make a comparison between DMM in [11] and MCC.

Fig. 9(a) and (b) shows the working process of DMM and MCC with the power generation ratios ranging from $(k_A^*/k_B^*/k_C^* = 0.8/1/1.2)$ to $(k_A^*/k_B^*/k_C^* = 1.2/1/0.8)$, and partial waveforms of $k_{\rm B}$ are enlarged to highlight their characteristics.

It can be seen that both DMM and MCC can achieve high precision in controlling dc power with the maximal deviation less than 0.005. Compared with DMM, the convergence speed of MCC is relatively slow; $k_{\rm B}$ in MCC fluctuates around the expected value during the time from 0.25 to 0.3 s. However, $k_{\rm B}$ in MCC can be stabilized to 1 during the time 0.75–0.8 s, as can be seen from Fig. 9(b). This means that the deviation will become smaller along with time. In Fig. 9(a), however, $k_{\rm B}$ in DMM still deviates from the expected value during the time 0.75–0.8 s. This is because the DMM uses the power of grid

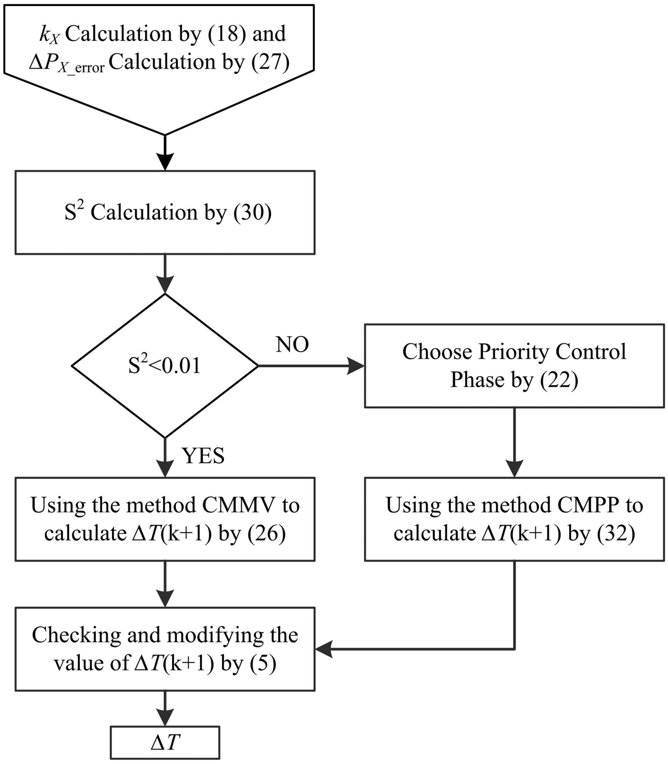

Fig. 8. Flow chart of method MCC.

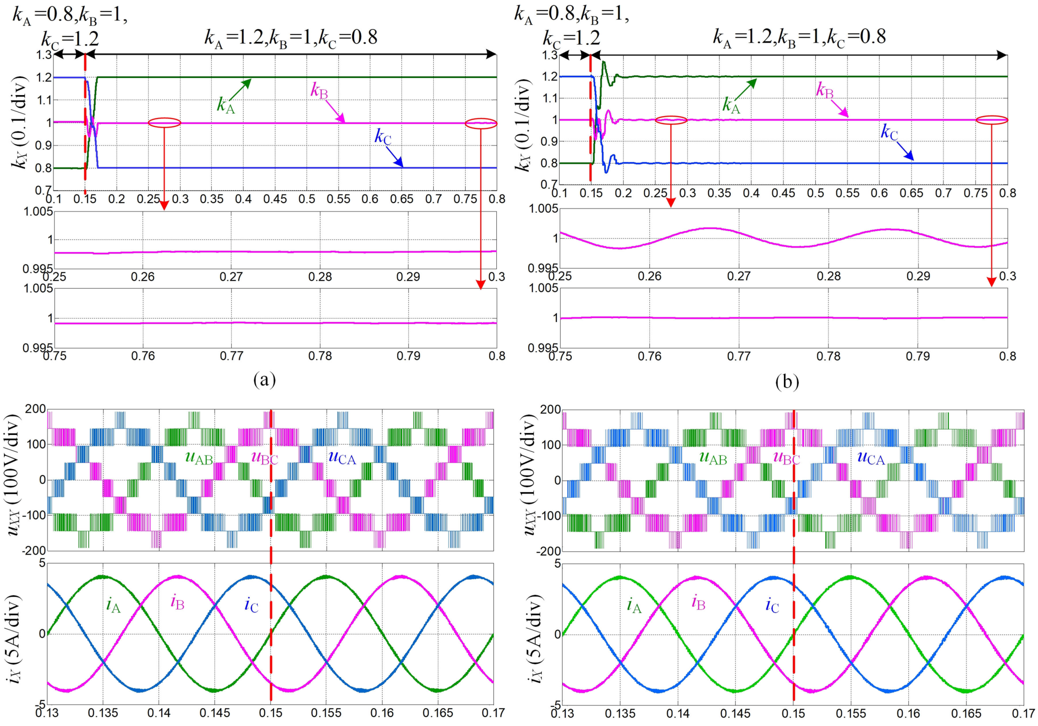

(a) (b)

(c) (d)

Fig. 9. Simulation results under $L = 4$mH. (a)–(b) Power generation ratios k_X with DMM and MCC, respectively. (c)–(d) Converter output voltages u_{XX} and output ac currents i_X with DMM and MCC, respectively.

side instead of the converter side, so the reactive power raised by the L-filter is unnecessary included in the calculation. Such difference tends to be small as the value of the L-filter is small. Still this will lead to error while controlling the power of the three phases. It will be worse when the L-filter is large under certain circumstances. In MCC, the output dc power is completely calculated by the converter side, so the power generation ratios can reach and stabilize at the given values. Fig. 9(c) and (d) shows the simulation results of converter output voltages u_{XX} and grid currents i_X. The high-quality output voltages and currents verify the effectiveness of DMM and MCC for dc power control.

In order to verify the cause of the power deviation in DMM, the simulation is implemented with the value of L-filter impedance increasing from 4 to 8 mH, while the other conditions remain unchanged. The results are shown in Fig. 10. It can be seen from Fig. 10(a) that the deviation of k_{B} in DMM is close to 0.01 during the time 0.25–0.3 s, which is much bigger than that under L = 4 mH, and k_{B} still has a deviation of approximately 0.005 at 0.75 to 0.8 s, meaning that it cannot reach the expected value. In MCC, the maximum deviation of k_{B} is less than 0.005 at 0.25 to 0.3 s, and k_{B} can stabilize at the expected values during the time 0.75–0.8 s, as shown in Fig. 10(b). Fig. 10(c) and (d) shows that the output line-to-line voltages and three-phase currents in both DMM and MCC are not affected as L increases. The simulation results indicate that the deviation of dc power in DMM will increase as L increases. It can be concluded that the dc power calculated by DMM is inaccurate.

B. Experimental Results and Analysis

1) Experimental Results of Three Interphase Power Control Methods (CMMM, CMPP, and CMMV): A downscale grid-connected inverter is developed in lab to verify the performance both in dynamic and steady states of proposed three methods. The parameters are the same as Table I. The filter available in our laboratory is an L-filter, whose impedance is a little larger than expected. Since the per-unit design is used in the lower power system in the experiment, its transfer function can represent and is also applicable to its count part in high power system. The control methods are implemented by TMS320F28335 with Xilinx FPGA, with the reference value of $i*_{\mathrm{d}}$4A, the output active power about 465 W, and the modulation index *m* about 0.89. Fig. 11(a)–(c) shows the whole working process of three PCMs with the power generation ratios ranging from $(k^*_A/k^*_B/k^*_C = 0.8/1/1.2)$ to $(k^*_A/k^*_B/k^*_C = 1.2/1/0.8)$. It can be seen that the power generation ratios of three control methods can reach the expected value accurately, where CMMM and CMPP take about 20 ms to reach the steady state after the power generation ratios are switched, while CMMV takes about 80 ms. Fig. 11(d)–(f) shows the waveforms of correction time ΔT calculated by three methods in the steady state. Similar to the simulation results, the waveforms of ΔT in CMMM and CMPP are discontinuous and switch between the maximum and minimum values. In CMMV, ΔT is a continuous value and is restricted within the limit values, indicating that CMMV can achieve the smooth control of dc power. Fig. 11(g)–(i) shows the

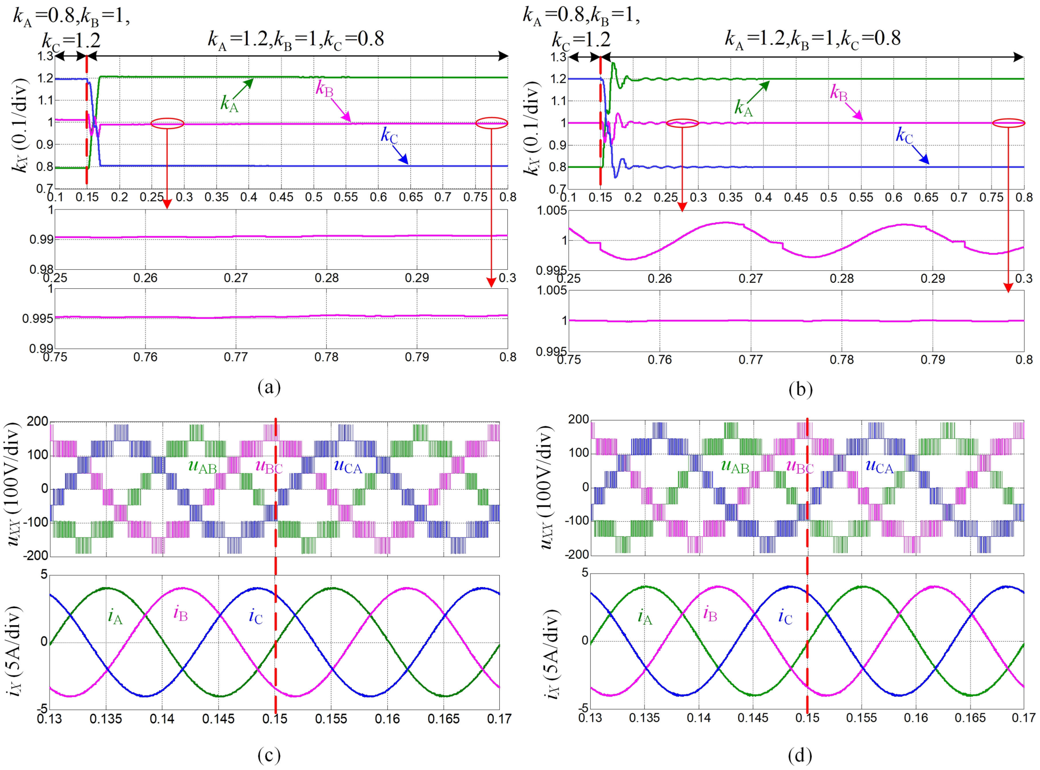

Fig. 10. Simulation results under $L = 8$mH. (a)–(b) Power generation ratios k_X with DMM and MCC, respectively. (c)–(d) Converter output voltages u_{XX} and output ac currents i_X with DMM and MCC, respectively.

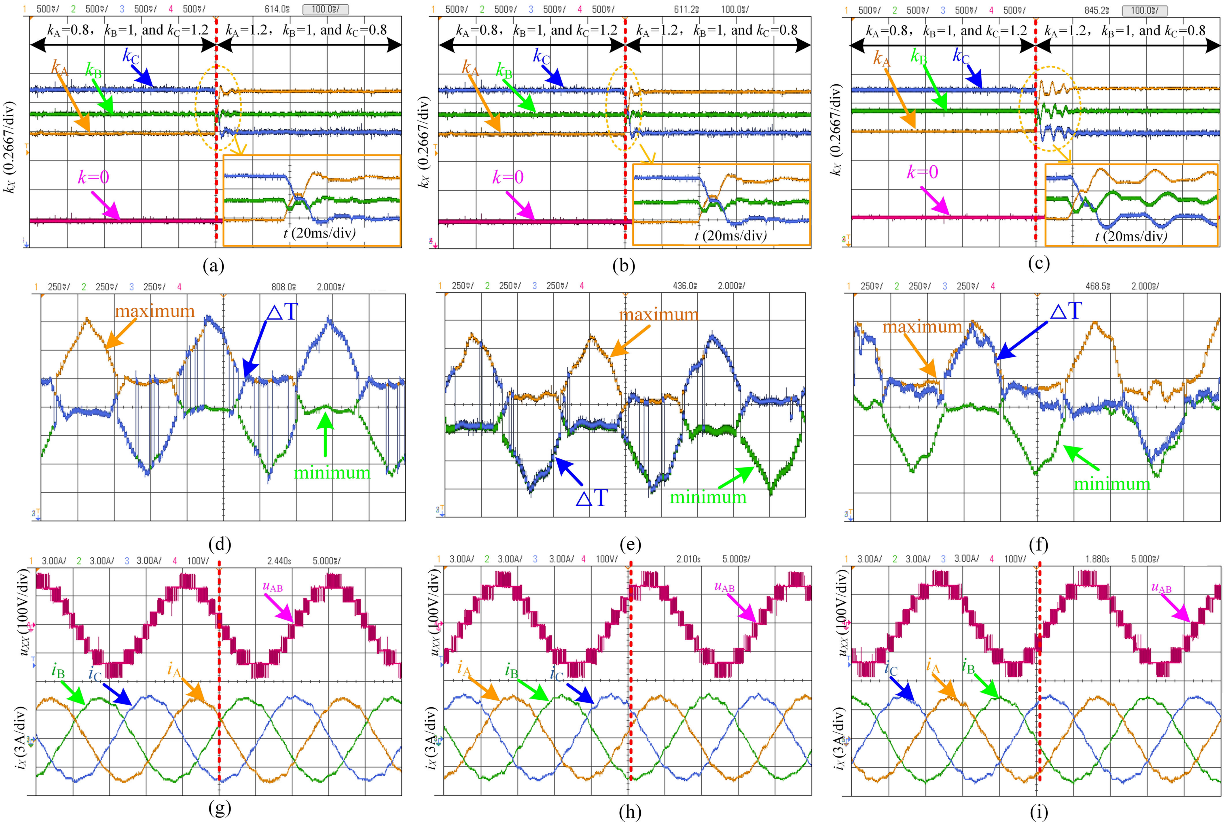

Fig. 11. Experimental results of CMMM, CMPP, and CMMV, respectively. (a)–(c) Power generation ratios k_X. (d)–(f) Steady-state waveform of ΔT. (g)–(i) Converter output voltage $u_{\rm AB}$ and output ac currents i_X.

waveforms of line-to-line voltage u_{AB} and three-phase currents i_X in the ac side of the inverter system. The figure shows that balanced ac currents can be obtained as power generation ratios change. However, the ac currents i_X are distorted slightly in the overall waveforms. That is because the capacity of the experimental platform is small as 465 VA, which is easily interfered by saturation voltage of IGBT, lead-acid battery impedance, etc.

2) Experimental Results of the Interphase Power Control Method Which Merged CMMV and CMPP (MCC): In order to examine the interphase power control of the MCC with imbalanced voltages, an experiment on five-level inverters is carried out. An adjustable dc voltage source available in our lab is used as the substitute of the upper battery module in phase C. The output voltage of this equipment is changed manually during the experiment. Meanwhile, the power generation ratios are changed from $(k_A^*/k_B^*/k_C^* = 1.3/1/0.7)$ to $(k_A^*/k_B^*/k_C^* = 1/0.7/1.3)$.

Fig. 12(a) shows the overall waveforms of three-phase power generation ratios k_{A}, k_{B}, and k_{C}, the output voltage $u_{\mathrm{out\_C1}}$ of the upper module in phase C, the current of adjustable voltage source in phase C $i_{\mathrm{dc\_C1}}$, the battery current of lower module in phase C $i_{\mathrm{dc\_C2}}$, and three-phase currents i_{A}, i_{B}, and i_{C} of the power grid side. Fig. 12(b)–(d) is partial enlarged images of red dotted frames (1)–(3) in Fig. 12(a), respectively. In Fig. 12(a), k_{A}, k_{B}, and k_{C} change 10 times from 1.3, 1, and 0.7 to 1, 0.7, and 1.3, respectively, where k_{A} and k_{B} decrease by 0.03 and k_{C} increases by 0.06 each time. The voltage of the adjustable voltage source in phase C increases gradually from 40 to 56 V manually. Compared with the rated battery module voltage 48 V in the system, the voltage changing rate is ±16.7%. It can be seen from Fig. 12(a) that the amplitude of $u_{\mathrm{out^{\cdot}C1}}$ is increasing continuously. In Fig. 12(a), the three waveforms are synchronized, as can be seen from the waveform of k_{C}. The measured average values of k_{A}, k_{B}, and k_{C} in Fig. 12(b)–(d) shows the power generation ratios k_{A}, k_{B}, and k_{C} finally reach the set values of 1, 0.7, and 1.3 within the tolerance of measurement error, which also indicates that power generation ratios between phases can be well controlled. Fig. 12(c) is partial enlarged images of the continuously change of power generation ratios between phases. k_{A}, k_{B}, and k_{C} reach the stable state after about 25 ms. It is thus concluded that the MCC obtains better performance both in dynamic and steady states.

The amplified waveforms of the three-phase currents of the grid side in Fig. 12(b)–(d) show that the balanced three-phase ac currents can still be obtained, as power generation ratios between phases and the module voltage change simultaneously. Therefore, the change of the power generation ratios between phases and the module voltage has no effect on the three-phase ac currents. As can be seen from Fig. 12(b) and (d), with the increase of module voltage, the power generation ratios between phases remains stable at the given value, indicating that the change of module voltage has no effect on the power generation ratios between phases. It also proves that the control strategy is also applicable under imbalanced module voltage conditions. In Fig. 12(b)–(d), the measured average value of the current $i_{\mathrm{dc\_C1}}$ of the upper module in phase C remains unchanged. The measured average value of the battery current $i_{\mathrm{dc\_C2}}$ of the lower module increases along with the k_{C}. The $u_{\mathrm{out\_C1}}$ waveform is close to square wave, which indicates that the module of phase C is always in P or N state in each carrier cycle with the changes of k_{C}. Therefore, as the k_{C} changes, the distribution of inter-phase power can only be satisfied by adjusting the conduction time of the lower module in phase C. That is, the change of k_{C} is represented by the change of $i_{\mathrm{dc\_C2}}$ in the experiment.

3) Inner-Phase Power Control Experimental Results: The inner-phase power control is the redistribution of dc power between submodules. An experiment on five-level inverters is carried out on the condition of $k_A^* = k_B^* = k_C^* = 1$, to verify the suitability of the inner-phase control strategy to voltage unbalance conditions and the continuous variability of the inner-phase power distribution. An adjustable voltage source is used as a substitute of the upper module battery of phase C in the experiment.

Fig. 13(a) shows the overall waveforms of the changes of inner-phase power coefficients l_{A1}, l_{B1}, and l_{C1}, the output voltage $u_{\mathrm{out\_C1}}$ of upper module in phase C, the current of upper module on phase C $i_{\mathrm{dc\_C1}}$, the battery current of lower module on phase C $i_{\mathrm{dc\_C2}}$, and three-phase currents i_{A}, i_{B}, and i_{C} on the power grid side. Fig. 13(b)–(d) are partial enlarged images of red dotted frames (1)–(3) in Fig. 13(a), respectively. In Fig. 13(a), l_{A1}, l_{B1}, and l_{C1} changed five times from 1.4, 1.2, and 0.8 to 1.2, 0.8, and 1.2, respectively, where l_{A1} decreases by 0.04, l_{B1} decreases by 0.08, and l_{C1} increases by 0.08 each time. The voltage of the adjustable voltage source in phase C increases gradually from 40 to 56 V manually. Compared with the rated battery module voltage 48 V in the system, the voltage changing rate is ±16.7%. It can be seen from Fig. 13(a) that the amplitude of $u_{\mathrm{out\_C1}}$ is increasing continuously, indicating the continuous rising of the battery voltage. The three waveforms in Fig. 13(a) are synchronized, as can be seen from the waveform of l_{C1}. The measured average values of l_{A1}, l_{B1}, and l_{C1} in Fig. 13(b)–(d) show that inner-phase power coefficients l_{A1}, l_{B1}, and l_{C1} finally reach the set values of 1.2, 0.8, and 1.2 within the tolerance of measurement error, which also proves that the inner-phase power coefficients are well controlled. From the waveforms of l_{A1}, l_{B1}, and l_{C1} in Fig. 13(c), it is thus concluded that the control strategy obtains good performance both in dynamic and steady states.

The amplified waveforms of the three-phase currents on the grid side in Fig. 13(b)–(d) show that the balanced three-phase ac currents can still be obtained, as the inner-phase power coefficients and the battery voltage change simultaneously. This proves that the change of the inner-phase power coefficients and the battery voltage has no effect on the three-phase ac currents. As can be seen from Fig. 13(b) and (d), with the increase of battery voltage, the inner-phase power coefficients remain stable at a given value. Therefore, the change of battery voltage has no effect on the inner-phase power coefficients, and it also indicates that the inner-phase power control strategy is applicable to imbalanced module voltage. In Fig. 13(b)–(d), the measured average value of the battery current $i_{\mathrm{dc\_C2}}$ of phase C changes from 2.507 to 2.024 A, and finally to 1.564 A. The battery voltage of the lower module in phase C remains unchanged, indicating that the battery output power of lower module in phase C decreases along with the increase of l_{C1}.

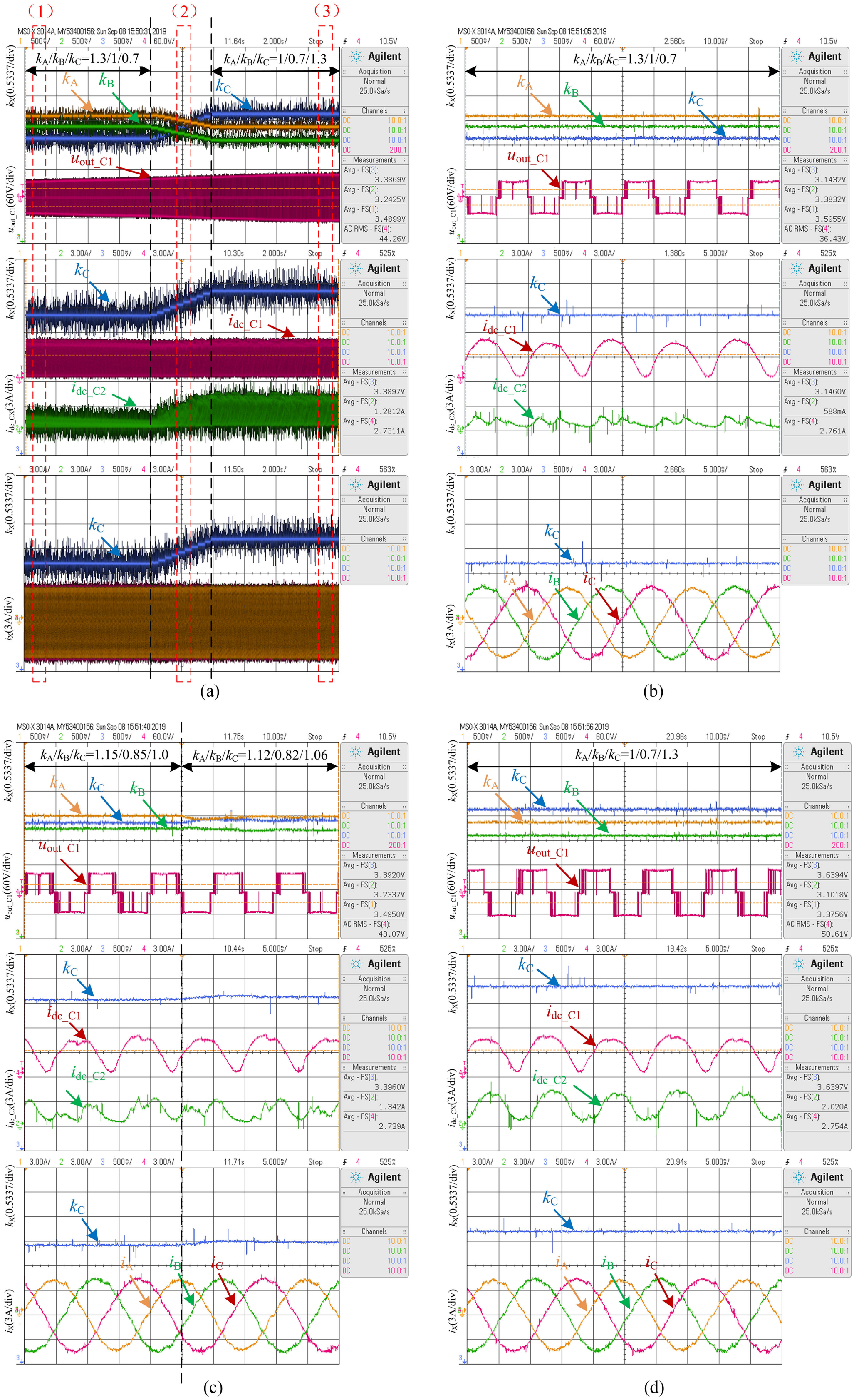

Fig. 12. Experimental results of MCC with power generation ratios ranging from $(k_A^*/k_B^*/k_C^* = 1.3/1/0.7)$ to $(k_A^*/k_B^*/k_C^* = 1/0.7/1.3)$. (a) Overall waveforms. (b)–(d) Partial enlarged images of red dotted frames (1), (2), and (3) in Fig 12(a).

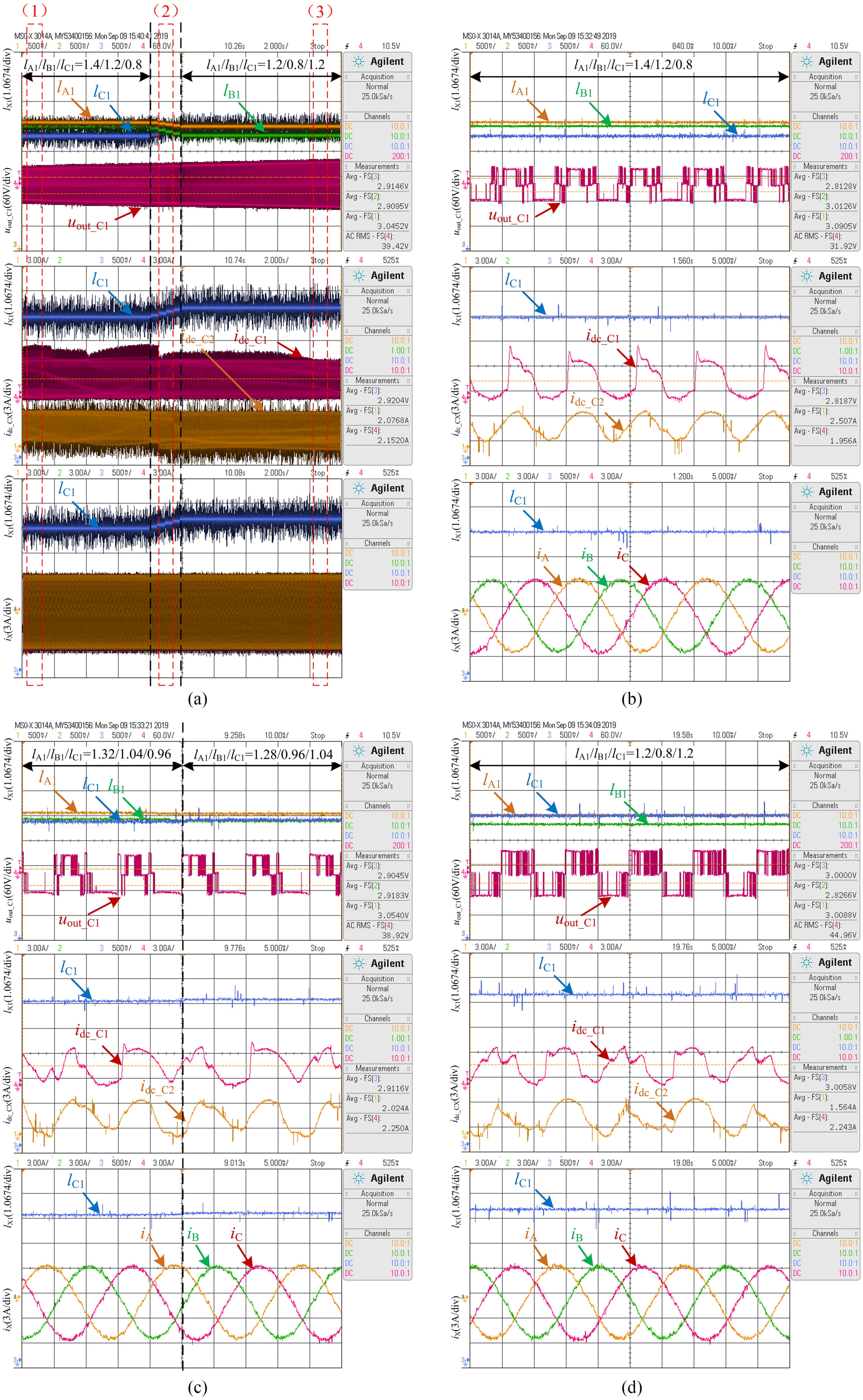

Fig. 13. Experimental results of MCC with inner-phase power coefficients ranging from ($l^*_{A1}/l^*_{B1}/l^*_{C1}$ = 1.4/1.2/0.8) to ($l^*_{A1}/l^*_{B1}/l^*_{C1}$ = 1.2/0.8/1.2). (a) Overall waveforms. (b)–(d) Partial enlarged images of red dotted frames (1), (2), and (3) in Fig 13(a).

However, the total output power of C-phase remains unchanged, so the output power of C-phase upper module increases, exactly conforming to the change of l_{C1}.

VII. CONCLUSION

In order to improve the efficiency of PV and energy storage systems, three novel interphase PCMs are proposed in this article to control the distribution of three-phase power. All the three interphase PCMs, CMMM, CMPP, CMMV, can control the dc power in both low and high power systems, though with their different performances in dynamic and steady states. Based on the study of their differences, the MCC, which combines the advantages of CMPP and CMMV, is proposed to achieve optimal control of interphase power. The performance of MCC is proven to be as dynamic as that of CMPP, and its performance in steady-state matches that of CMMV. To further improve the power control capability of CHB, the inner-phase PCM is then proposed to achieve precise power control of each submodule. Results of the simulation and experimental show that both the interphase and inner-phase PCMs can achieve good power control even under imbalanced voltages and can acquire balanced three-phase currents, indicating that the proposed PCMs are both practical and effective in controlling the power distribution.

REFERENCES

[1] J. Chavarria, D. Biel, F. Guinjoan, C. Meza, and J. J. Negroni, “Energy-balance control of PV cascaded multilevel grid-connected inverters under level-shifted and phase-shifted PWMs,” *IEEE Trans. Ind. Electron.*, vol. 60, no. 1, pp. 98–111, Jan. 2013.

[2] J. Sastry, P. Bakas, H. Kim, L. Wang, and A. Marinopoulos, “Evaluation of cascaded H-bridge inverter for utility-scale photovoltaic systems,” *Renewable Energy*, vol. 69, pp. 208–218, Sep. 2014.

[3] D. Sun *et al.*, “Modeling, impedance design, and efficiency analysis of quasi-Z source module in cascaded multilevel photovoltaic power system,” *IEEE Trans. Ind. Electron.*, vol. 61, no. 11, pp. 6108–6117, Nov. 2014.

[4] L. Liu, H. Li, Y. Xue, and W. Liu, “Reactive power compensation and optimization strategy for grid-interactive cascaded photovoltaic systems,” *IEEE Trans. Power Electron.*, vol. 30, no. 1, pp. 188–202, Jan. 2015.

[5] C. D. Townsend, T. J. Summers, and R. E. Betz, “Phase-shifted carrier modulation techniques for cascaded H-bridge multilevel converters,” *IEEE Trans. Ind. Electron.*, vol. 62, no. 11, pp. 6684–6696, Nov. 2015.

[6] A. Marzoughi, R. Burgos, D. Boroyevich, and Y. Xue, “Investigation and comparison of cascaded H-bridge and modular multilevel converter topologies for medium-voltage drive application,” in *Proc. 40th Annu. Conf. IEEE Ind. Electron. Soc.*, Dallas, TX, USA, 2014, pp. 1562–1568.

[7] A. Marzoughi, R. Burgos, D. Boroyevich, and Y. Xue, “Design and comparison of cascaded H-bridge, modular multilevel converter, and 5-L active neutral point clamped topologies for motor drive applications,” *IEEE Trans. Ind. Appl.*, vol. 54, no. 2, pp. 1404–1413, Mar./Apr. 2018.

[8] M. Malinowski, K. Gopakumar, J. Rodriguez, and M. A. Perez, “A survey on cascaded multilevel inverters,” *IEEE Trans. Ind. Electron.*, vol. 57, no. 7, pp. 2197–2206, Jul. 2010.

[9] Y. Yu, G. Konstantinou, B. Hredzak, and V. G. Agelidis, “Operation of cascaded H-bridge multilevel converters for large-scale photovoltaic power plants under bridge failures,” *IEEE Trans. Ind. Electron.*, vol. 62, no. 11, pp. 7228–7236, Nov. 2015.

[10] Y. Yu, G. Konstantinou, B. Hredzak, and V. G. Agelidis, “Optimal zero sequence injection in multilevel cascaded H-bridge converter under unbalanced photovoltaic power generation,” in *Proc. Int. Power Electron. Conf.*, Hiroshima, Japan, 2014, pp. 1458–1465.

[11] Y. Yu, G. Konstantinou, B. Hredzak, and V. G. Agelidis, “Power balance of cascaded H-bridge multilevel converters for large-scale photovoltaic integration,” *IEEE Trans. Power Electron.*, vol. 31, no. 1, pp. 292–303, Jan. 2016.

[12] Y. Yu, G. Konstantinou, B. Hredzak, and V. G. Agelidis, “Power balance optimization of cascaded H-bridge multilevel converters for large-scale photovoltaic integration,” *IEEE Trans. Power Electron.*, vol. 31, no. 2, pp. 1108–1120, Feb. 2016.

[13] Q. Wu, X. Sun, Y. Hao, E. Chen, and B. Wang, “A SoC control strategy based on wireless droop control for energy storage systems in ac islanded microgrid,” in *Proc. IEEE 8th Int. Power Electron. Motion Control Conf.*, Hefei, China, 2016, pp. 2893–2898.

[14] Y. Yu, G. Konstantinou, B. Hredzak, and V. G. Agelidis, “On extending the energy balancing limit of multilevel cascaded H-bridge converters for large-scale photovoltaic farms,” in *Proc. Australas. Univ. Power Eng. Conf.,* Hobart, TAS, Australia, 2013, pp. 1–6.

[15] B. Xiao, K. Shen, J. Mei, F. Filho, and L. M. Tolbert, “Control of cascaded H-bridge multilevel inverter with individual MPPT for grid-connected photovoltaic generators,” in *Proc. IEEE Energy Convers. Congr. Expo.*, Raleigh, NC, USA, 2012, pp. 3715–3721.

[16] S. Rivera, S. Kouro, B. Wu, J. I. Leon, J. Rodríguez, and L. G. Franquelo, “Cascaded H-bridge multilevel converter multistring topology for large scale photovoltaic systems,” in *Proc. IEEE Int. Symp. Ind. Electron.*, Gdansk, Poland, 2011, pp. 1837–1844.

[17] B. Xiao, L. Hang, J. Mei, C. Riley, L. M. Tolbert, and B. Ozpineci, “Modular cascaded H-bridge multilevel PV inverter with distributed MPPT for grid-connected applications,” *IEEE Trans. Ind. Appl.*, vol. 51, no. 2, pp. 1722–1731, Mar./Apr. 2015.

[18] S. Rivera, B. Wu, S. Kouro, H. Wang, and D. Zhang, “Cascaded H-bridge multilevel converter topology and three-phase balance control for large scale photovoltaic systems,” in *Proc. 3rd IEEE Int. Symp. Power Electron. Distrib. Gener. Syst.*, Aalborg, Denmark, 2012, pp. 690–697.

[19] R. P. Aguilera *et al.*, “Predictive control of cascaded H-bridge converters under unbalanced power generation,” *IEEE Trans. Ind. Electron.*, vol. 64, no. 1, pp. 4–13, Jan. 2017.

[20] Z. Ye *et al.*, “A novel DC-power control method for cascaded H-bridge multilevel inverter,” *IEEE Trans. Ind. Electron.*, vol. 64, no. 9, pp. 6874–6884, Sep. 2017.

[21] R. Sharma and A. Das, “Per phase power balancing in grid connected cascaded H-bridge multilevel converter for solar PV application,” in *Proc. 6th Int. Conf. Comput. Appl. Elect. Eng.-Recent Adv.*, Roorkee, India, 2017, pp. 433–438.

[22] Z. Ye *et al.*, “Simplified PWM strategy for neutral-point-clamped (NPC) three-level converter,” *J. Power Electron.*, vol. 14, no. 3, pp. 519–530, Mar. 2014.

[23] Z. Ye, Y. Xu, X. Wu, G. Tan, X. Deng, and Z. Wang, “A simplified PWM strategy for a neutral-point-clamped (NPC) three-level converter with unbalanced DC links,” *IEEE Trans. Power Electron.*, vol. 31, no. 4, pp. 3227–3238, Apr. 2016.

Zongbin Ye (Member, IEEE) was born in Jiangxi, China, in 1983. He received the Ph.D. degree in electrical engineering from the China University of Mining and Technology, Xuzhou, China, in 2010.

Since 2015, he has been an Associate Professor with the School of Information and Electrical Engineering, China University of Mining and Technology, Xuzhou, China. He has authored several journal and conference articles and also one book in the area of motor control. His research interests include development of high-power multilevel converters and motor drivers.

Qisheng Zheng was born in Henan, China, in 1995. He received the B.S. degree in electrical engineering and automation from the Henan University of Technology, Zhengzhou, China, in 2018. He is currently working toward the M.S. degree in power electronics and drives with the China University of Mining and Technology, Xuzhou, China.

His research interests include power electronics and multilevel inverters.

Hanjun Pei was born in Hubei, China, in 1996. He received the B.S. degree in electrical engineering and automation from Hubei Normal University, Huangshi, China, in 2018. He is currently working toward the M.S. degree in power electronics and drives with the China University of Mining and Technology, Xuzhou, China.

His research interests include power electronics and multilevel inverters.

Josep M. Guerrero (Fellow, IEEE) received the B.S. degree in telecommunications engineering, M.S. degree in electronics engineering, and the Ph.D. degree in power electronics from the Technical University of Catalonia, Barcelona, Spain, in 1997, 2000, and 2003, respectively.

Since 2011, he has been a Full Professor with the Department of Energy Technology, Aalborg University, Aalborg, Denmark, where he is responsible for the Microgrid Research Program. Since 2014, he is a Chair Professor with Shandong University, Jinan, China; a Distinguished Guest Professor with Hunan University, Changsha, China, since 2015; and a Visiting Professor Fellow with Aston University, Aston, U.K., and a Guest Professor with the Nanjing University of Posts and Telecommunications, Nanjing, China, since 2016. From 2019, he became a Villum Investigator by The Villum Fonden, which supports the Center for Research on Microgrids, Aalborg University, Aalborg, Denmark, being the Founder and Director of the same center. He has authored or coauthored more than 500 journal papers in the fields of microgrids and renewable energy systems, which are cited more than 40 000 times. His research interests include different microgrid aspects, including power electronics, distributed energy-storage systems, hierarchical and cooperative control, energy management systems, smart metering, and the Internet of Things for ac/dc microgrid clusters and islanded minigrids, specially focused on microgrid technologies applied to offshore wind and maritime microgrids for electrical ships, vessels, ferries, and seaports.

Prof. Guerrero is an Associate Editor for a number of IEEE TRANSACTIONS. He was the recipient of the Best Paper Award of the IEEE TRANSACTIONS ON ENERGY CONVERSION for the period 2014–2015, and the Best Paper Prize of IEEE-PES, in 2015. Also, he was recipient of the Best Paper Award of the *Journal of Power Electronics*, in 2016. During six consecutive years, from 2014 to 2019, he was awarded by Clarivate Analytics (former Thomson Reuters) as Highly Cited Researcher. In 2015, he was elevated as IEEE Fellow for his contributions on “distributed power systems and microgrids.”

Shiqi Mao was born in Jiangsu, China, in 1994. He received the B.S. degree in electrical engineering and automation from Suzhou University of Science and Technology, Suzhou, China, in 2017. He is currently working toward the M.S. degree in power electronics and drives with the China University of Mining and Technology, Xuzhou, China.

His research interests include power electronics and multilevel inverters.

Tingting Wang was born in Zhejiang, China, in 1994. She received the B.S. degree in electrical engineering and automation from Wuhan Textile University, Wuhan, China, in 2017. She is currently working toward the M.S. degree in power electronics and drives with the China University of Mining and Technology, Xuzhou, China.

Her research interests include power electronics and multilevel inverters.

Anni Chen was born in Zhejiang, China, in 1993. She received the B.S. degree in electrical engineering and automation from the Zhejiang University of Technology, Zhejiang, China, in 2016, and the M.S. degree in power electronics and drives from the China University of Mining and Technology, Xuzhou, China, in 2019.

She is currently working with the Zhongtian Construction Group Co., Ltd., Hangzhou, China. Her research interests include power electronics and multilevel inverters.

Zhiguo Zhang was born in Shandong, China, in 1992. He received the B.S. degree in electrical engineering and automation from North west A&F University, Xianyang, China, in 2015, and the M.S. degree in power electronics and drives from the China University of Mining and Technology, Xuzhou, China, in 2018.

He is currently working with the State Grid Yantai Power Supply Company, Yantai, China. His research interests include power electronics and multilevel inverters.

Linlin Jiang was born in Anhui, China, in 1992. He received the B.S. degree in electrical engineering and automation from the Anhui University of Science and Technology, Huainan, China, in 2015, and the M.S. degree in power electronics and drives from the China University of Mining and Technology, Xuzhou, China, in 2018.

He is currently working with the State Grid Jiaxing Power Supply Company, Jiaxing, China. His research interests include power electronics and multilevel inverters.

Dongsheng Yu (Member, IEEE) received the B.Eng. and Ph.D. degrees in electrical engineering from the School of Information and Electrical Engineering, China University of Mining and Technology, Xuzhou, China, in 2005 and 2011, respectively.

He is currently an Associate Professor with the School of Information and Electrical Engineering, China University of Mining and Technology. From 2009 to 2010, he was a Visiting Student with the University of Western Australia, Crawley, WA, Australia, where he was an Endeavour Fellow, in 2014. He has authored or coauthored one book and more than 30 papers in these areas. His research interests include power electronics, renewable energy, electric drives, nonlinear dynamics, and memristive systems.

Tyrone Fernando (Senior Member, IEEE) received the B.Eng.(hons.) degree in electrical engineering and the Ph.D. degree in biomedical engineering from the University of Melbourne, Melbourne, VIC, Australia, in 1990 and 1996, respectively.

In 1996, he was with the School of Electrical Electronic and Computer Engineering, University of Western Australia, Crawley, WA, Australia, where he is currently a Professor, where he was the Deputy Head, from 2009 to 2010. He has authored several journal and conference articles and also two books in the areas of functional observers and closed-loop control of blood glucose in diabetics. His research interests include estimations theory, control theory, and application of control theory to smart grids, power systems, circuits and systems, and biomedical engineering.

Prof. Fernando was an Associate Editor for the IEEE TRANSACTIONS ON INFORMATION TECHNOLOGY IN BIOMEDICINE and a Guest Editor for the Optimal Control Applications and Methods. He has also been an Associate Editor for TCAS II. He is currently an Associate Editor for the IEEE TCAS I and IEEE Access.